

X-ray Diffraction and X-ray Absorption Spectroscopy Studies on the Chemical Transformation and Formation of Nanoscale $\text{LaMnO}_{3.12}$

Xing Chen, Quan Cai, Wei Wang, Zhongjun Chen, Zhonghua Wu,* and Ziyu Wu

Beijing Synchrotron Radiation Facility, Institute of High Energy Physics, CAS, 100049 Beijing, China and Graduate School of the Chinese Academy of Sciences, 100864 Beijing, China

Caihong Feng and Qianshu Li

College of Chemical Engineering and Materials Science, Beijing Institute of Technology, P. O. Box 327, Beijing 100081, People's Republic of China

Received: October 11, 2006; In Final Form: December 24, 2006

Nanoscale lanthanum manganites ($\text{LaMnO}_{3+\delta}$) were prepared with thermal decomposition of precursors derived from hydrothermal synthetic method. Transmission electron microscopy (TEM) and X-ray diffraction (XRD) revealed that the as-prepared sample is composed of nanofilaments in an amorphous form. The as-prepared nanoparticles were hydrothermally treated at 180 °C for 12 h and then were annealed at 600, 800, and 900 °C for 4 h to form $\text{LaMnO}_{3+\delta}$. With increasing annealing temperature, a shape change from filaments to rods to spheres was found, and their diameters increased from 4.5 to 52.9 nm. XRD showed a chemical transformation from $\text{La}(\text{OH})_3$ to $\text{LaMnO}_{3+\delta}$. Extended X-ray absorption fine structure (EXAFS) and X-ray absorption near-edge structure (XANES) are used to investigate the change of the local atomic structure around La/Mn with increasing annealing temperature. Combining the TEM, XRD, XANES and EXAFS results, the La-compound is found to be embedded in an amorphous Mn compound with medium range order. As annealed at different temperature, the chemical transformation process from $\text{La}(\text{OH})_3$ to $\text{LaMnO}_{3+\delta}$ was discussed. It was the chemical transformation that drives the shape change of these nanomaterials.

Introduction

Recently, perovskite-type metal oxides (general formula ABO_3) have attracted considerable interests due to their chemical activity, thermal stability in the catalytic total oxidation of hydrocarbons,^{1–3} and potential commercial applications as combustion, fuel cell electrodes, gas detection sensors, and so on.^{4–7} In particular, manganese-based perovskite oxides have shown a great variety of magnetic and transport properties that strongly depend on the stoichiometric amount of oxygen (formula $\text{LaMnO}_{3+\delta}$) and the local atomic structures. $\text{LaMnO}_{3.07}$ is a ferromagnetic compound with neither metal–insulator transition nor giant magnetoresistance, while $\text{LaMnO}_{3.15}$ is a magnetically inhomogeneous compound showing spin-glass-like behavior at a low temperature.⁹ The excess oxygen cannot be accommodated and results in an equal amount of La and Mn vacancies as argued by van Roosmalen et al.^{10–11} Much theoretical and experimental research has been reported on the distortion of oxygen octahedron.⁹

A great deal of work has been done regarding $\text{LaMnO}_{3+\delta}$ compounds, and a continuous evolution from the highly distorted orthorhombic structure in $\delta = 0$ toward a rhombohedral structure in $\delta = 0.15$ sample has been found.¹² There is still less known for the structures of nanoscale $\text{LaMnO}_{3+\delta}$ compounds. However, their potential application promotes us to study the local atomic structure. In this work, the nanoscale $\text{LaMnO}_{3+\delta}$ was synthesized by chemical methods and characterized by transmission electron microscope (TEM), X-ray diffraction (XRD), and extended X-ray absorption fine structure (EXAFS) spectroscopy. When

these techniques were combined, the formation process from the as-prepared sample to $\text{LaMnO}_{3+\delta}$ was discussed, and their lattice parameters and atomic coordinates were also suggested. The local atomic structural dependence on the shape and sizes was also discussed in the paper.

Experimental

Sample Preparation. Nanoscale $\text{LaMnO}_{3+\delta}$ oxides were prepared by thermal decomposition of precursors derived from hydrothermal synthetic methods. The synthesis details are as follows: First, 5 mmol $\text{La}(\text{NO}_3)_3 \cdot 6\text{H}_2\text{O}$ was dissolved in quantities of distilled water, then 50% $\text{Mn}(\text{NO}_3)_3$ solution was added. Second, with an intense stirring, KOH solution was rapidly dropped into the solution in a molar ratio of $\text{La}(\text{NO}_3)_3 \cdot 6\text{H}_2\text{O} / \text{Mn}(\text{NO}_3)_3 / \text{KOH} = 1:1:6$. A white precipitate appeared immediately. Third, after stirring for about 10 min the precipitate was divided into two groups. One was collected and washed with deionized water and absolute alcohol and was dried at 60 °C; this was denoted as sample (a). The other was transferred into a 50 mL autoclave that was filled with deionized water up 80% of the total volume, and heated at 180 °C for about 12 h. The sample was collected by filtration and washed with deionized water and absolute alcohol to remove any possible ionic remnants and was dried in air at 60 °C; this was denoted as sample (b). Finally, the $\text{LaMnO}_{3+\delta}$ perovskite oxides were respectively obtained by annealing sample (b) at 600, 800, and 900 °C for 4 h; these samples were denoted as sample (c), (d), and (e), respectively.

Sample Characterization. XRD and X-ray absorption spectra (XAS) were recorded at beam line 4B 9A of Beijing

* Corresponding author. E-mail: wuzh@ihep.ac.cn.

Synchrotron Radiation Facility (BSRF). The storage ring was run at 2.2 GeV with an average electron current of 80 mA and the X-ray was monochromatized by a double-crystal Si (111) monochromator. The EXAFS spectra of La L_3 -edge and Mn K-edge were recorded at room temperature in transmission mode. The powder samples were homogeneously smeared on the Scotch adhesive tape; more than two layers were folded to reach the optimum absorption thickness ($\Delta\mu d \approx 1$, $\Delta\mu$ is the absorption edge jump and d is the physical thickness of the sample). Incident and transmission X-ray intensities were detected and recorded, respectively, using ionization chambers that were installed in front of and behind the samples. The energy resolution ($\Delta E/E$) is about 3×10^{-4} .

EXAFS Data Analysis. EXAFS data were analyzed with the computer program WinXAS3.1.¹³ The energy thresholds were determined as the maxima of the first derivative. The absorption curves were normalized, and then the EXAFS spectra $\chi(k)$ were obtained after removal of the preedge and postedge background. The Fourier transform spectra (FTs) of La L_3 -edge and Mn K-edge were obtained for $k^3\chi(k)$ with a Bessel window in the range 3.3–9.7 \AA^{-1} for La L_3 -edge and 3.3–12.2 \AA^{-1} for Mn K-edge. The back-FT spectra of La L_3 -edge were performed in 1.25–2.60 \AA for samples (a) and (b) and 0.98–3.84 \AA for samples (c), (d), and (e). The independent fitting parameters calculated by using $N_{\text{ind}} = 2\Delta k\Delta R/\pi$ are 5.5 for the former and 11.7 for the latter. An R -range of 0.65–2.15 \AA was used in Mn K-edge for all samples and the number of independent parameters was calculated to be 8.5. Theoretical amplitude and phase-shift functions were calculated from $\text{La}(\text{OH})_3$ ¹⁴ and $\text{LaMnO}_{3+\delta}$ ¹⁵ crystalline structures by using FEFF7.¹⁶ Because of the transferability of the amplitude and phase shift, the coordination parameters of the unknown samples can be obtained by fitting the experimental curves with theoretical amplitudes and phase shifts.

Results and Discussion

TEM and XRD Results. These nanoscale materials were characterized by using TEM. As examples, the as-prepared sample (a) and samples (c), (d), and (e) are shown in Figure 1. It can be seen from Figure 1 that the as-prepared sample is composed of nanofilaments with the diameter of 4.5 nm. An inherent reason to form the nanofilaments is the habit of anisotropic growth.¹⁷ For these samples annealed below 600 °C, the filament-shape is dominant. But in the whole temperature range, these nanomaterials show a tendency of shape change from filament to rod to sphere, which implies that these nanofilaments gain enough energy from heating to activate the shape transformation. The diameters of the nanofilaments or the particle sizes were estimated to be 4.5, 4.5, 5.0, 26.0, and 52.9 nm for sample (a), (b), (c), (d), and (e), respectively, from TEM photographs.

Figure 2 shows the XRD patterns of these samples. For comparison, the XRD patterns of bulk $\text{La}(\text{OH})_3$ with $P6_3/m$ space group¹⁴ and $\text{LaMnO}_{3.12}$ with $R-3c$ space group¹⁵ are also shown in Figure 2. Obviously, there is no detectable diffraction peaks on sample (a), which means that the as-prepared sample is in an amorphous form without long-range order in its structure. The XRD peaks of sample (b) are co-incident with the crystalline $\text{La}(\text{OH})_3$ with $P6_3/m$ space group except for the broadening of diffraction peaks due to the smaller particle size. At the same time, the coincidence of peak positions also implies that these nanocrystalline $\text{La}(\text{OH})_3$ have almost the same lattice parameters with bulk counterparts. It is puzzling for us that there are no diffraction peaks being found from Mn compounds in

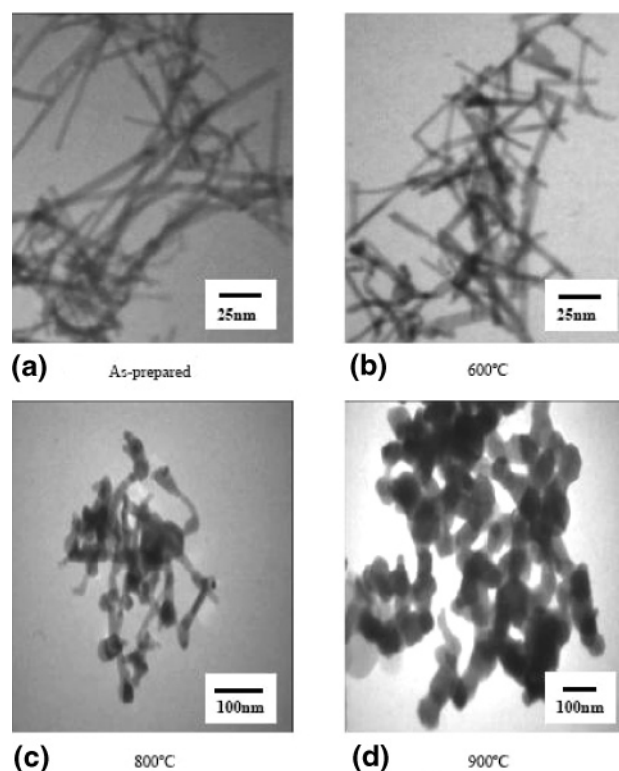


Figure 1. TEM photograph of sample (a) (panel a), (c) (panel b), (d) (panel c), and (e) (panel d). This shows a tendency of shape change from filament to rod to sphere.

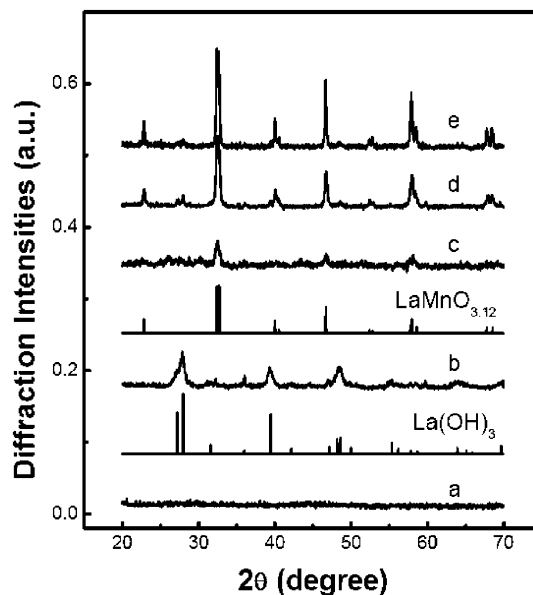


Figure 2. XRDs for the nanometer samples with $\lambda = 1.54 \text{ \AA}$. (a) As-prepared sample. (b), (c), (d), and (e) were hydrothermally treated at 180 °C for 12 h. Then, (c), (d), and (e) were annealed at 600, 800, and 900 °C, respectively, from (b) for 4 h.

the whole temperature range, but the FTs (see Figure 4) demonstrates clearly that sample (b) has an acceptable medium range order. Combining the two sides, we think that the Mn compound is in an amorphous state with medium range order. The crystalline $\text{La}(\text{OH})_3$ particles are embedded in this amorphous Mn-compound matrix, and the XRD patterns come from the central crystalline $\text{La}(\text{OH})_3$. When the sample was annealed above 600 °C, it had the same crystal structure as bulk $\text{LaMnO}_{3.12}$ with $R-3c$ space group except for a faint impurity peak located at about 27.8° , which was from the $\text{La}(\text{OH})_3$

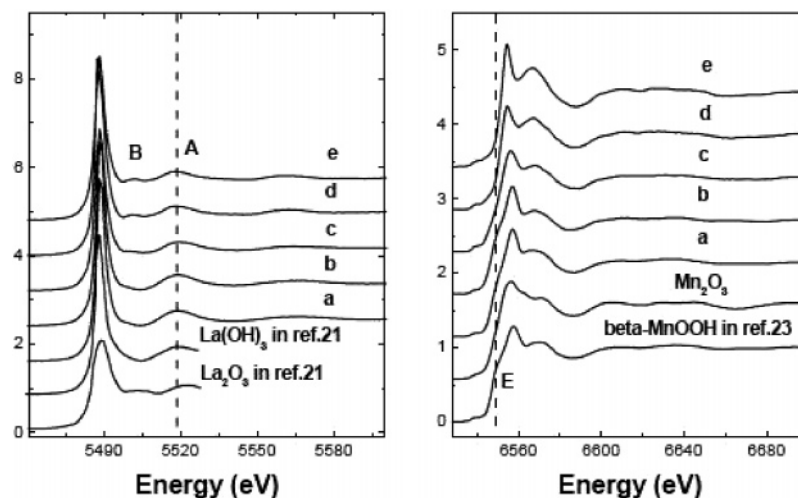


Figure 3. XANES spectra of La L₃-edge (left) and Mn-K edge (right). The XANES spectra of La₂O₃, La(OH)₃, β -MnOOH, and Mn₂O₃ in refs 21 and 23 are also shown and compared.

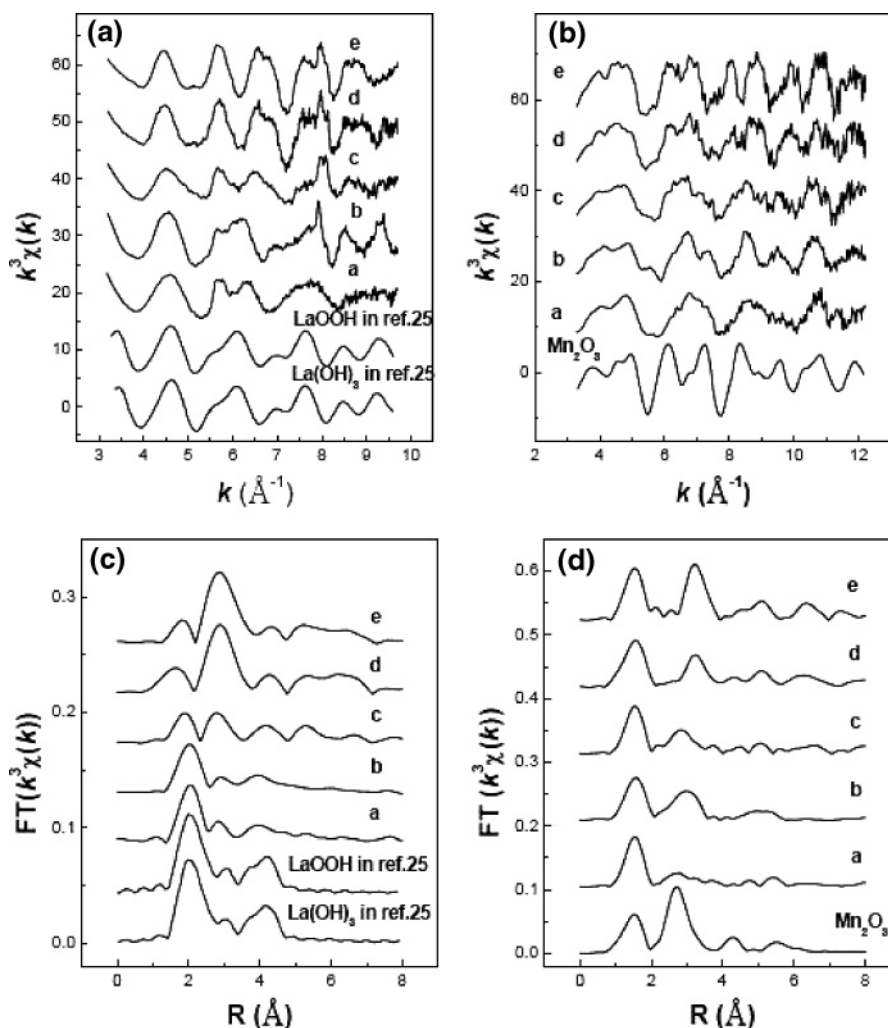


Figure 4. The k^3 -weighted EXAFS signals for La L₃-edge (a) and Mn K-edge (b) as well as the Fourier transform spectra of La L₃-edge (c) and Mn K-edge (d).

crystal. Evidently, all these samples, (c), (d), and (e), do not completely transform from the parent phase La(OH)₃ to the new phase LaMnO_{3,12}. As we know, La(OH)₃ can be transformed into La₂O₃ at above 600 °C,¹⁸ but we did not find any diffraction peaks from La₂O₃. This is because La₂O₃ is not very stable in air, and it is easy for it to absorb water from air to change back to La(OH)₃.¹⁹ On the other hand, the parent phase is not pure

La(OH)₃; it should include some Mn compound. As the La(OH)₃ was transformed to La₂O₃, most of it will react with Mn-compound to form the final phase LaMnO_{3,12}. The impurity diffraction peaks in samples (c), (d), and (e) illustrate that a minor part of La₂O₃ was not transformed into LaMnO_{3,12} then transformed back to La(OH)₃ when keeping at room temperature in air. With the annealing temperature increasing, diffraction

intensities increase and the diffraction peaks get sharpened, which demonstrates that the crystallite experiences a growing-up process. The diffraction peak of $\text{La}(\text{OH})_3$ in sample (e) is very weak, which means that the content of $\text{La}(\text{OH})_3$ in sample (e) is very low and can be ignored for EXAFS data analysis. We also note that the positions of the XRD peaks in sample (c), (d), and (e) are the same with almost no change with the annealing temperature, which means that they have the same lattice parameters in $R\text{-}3c$ space group. The lattice parameters of sample (e) can be calculated as $a = 5.523 \text{ \AA}$ and $c = 13.328 \text{ \AA}$ from its XRD pattern. In an earlier reference,²⁰ it was reported that LaMnO_3 can be obtained with the nonstoichiometric oxygen to form $\text{LaMnO}_{3+\delta}$ when annealed, and that the volume of $\text{LaMnO}_{3+\delta}$ unit cell decreases with increasing δ (e.g., $\delta = 0$ with $V = 367.4 \text{ \AA}^3$, $\delta = 0.07$ with $V = 357.3 \text{ \AA}^3$, and $\delta = 0.1$ with $V = 353.4 \text{ \AA}^3$).²⁰ The unit cell volume of the $\text{LaMnO}_{3+\delta}$ changes linearly with δ . Therefore, from the calculated volume of the unit cell for sample (e), 350.8 \AA^3 , we conclude that there are some cation vacancies in samples (c), (d) and (e) and $\delta \approx 0.12$.

When the TEM and XRD analysis from sample (a) to (c) are combined, their size and shape are almost the same. However in the annealing procedure, the crystallization of $\text{La}(\text{OH})_3$ and the chemical transformation from $\text{La}(\text{OH})_3$ to $\text{LaMnO}_{3+\delta}$ occurred. So we believe that the crystallization and the chemical transformation are carried out only in single nanofilaments without the reaction among different nanofilaments. Therefore, in the as-prepared sample La/Mn compounds coexist in each nanofilament. This also supports the conclusion that the La-compounds are covered by the Mn-compound in the as-prepared nanofilaments.

X-ray Absorption Near-Edge Structure (XANES) for La L_3 -Edge and Mn K-Edge. Normalized XANES spectra of the La L_3 -edge and Mn K-edge are shown in Figure 3. For La L_3 -edge, the XANES spectra consist of a strong "white line" followed by a main feature A. A weak feature B appears when the sample is annealed at above 600°C , which can be used to distinguish the LaOOH or $\text{La}(\text{OH})_3$ from La_2O_3 .²¹ The XANES of sample (a) and (b) is very similar to that of LaOOH or $\text{La}(\text{OH})_3$ in which feature B is absent²¹ (Figure 3, left panel). The feature A shifts toward lower energy with increasing annealing temperature, indicating the increase of average La–O distance in the first shell.²² For Mn K-edge, the preedge feature C, which is attributed to $\text{Mn}_{3d}\text{-O}_{2p}$ hybridization, does not change their position with annealing temperature. From the sample preparation, we know that the reaction of $\text{Mn}(\text{NO}_3)_3$ with KOH will produce MnOOH . The shoulder-like feature E that exists in sample (a) and (b) is also very similar to that of MnOOH ²³ (Figure 3, right panel), and it disappears completely when the annealing temperature is over 600°C , indicating that the MnOOH -like structure does not survive any more even if they do not transform to $\text{LaMnO}_{3+\delta}$ completely. Dish et al. reported that the MnOOH was decomposed to Mn_2O_3 at $350\text{--}400^\circ\text{C}$ ²⁴ at which feature E is absent.²³ This suggests that sample (c), (d), and (e) have been transformed into an Mn compound such as $\text{LaMnO}_{3+\delta}$ without MnOOH contribution. This has been confirmed by the XRD patterns as shown in Figure 2.

EXAFS Results. The k^3 -weighted EXAFS oscillations for La L_3 - and Mn K-edge are shown in Figure 4a,b. For comparison, the k^3 -weighted EXAFS signals for bulk Mn_2O_3 , $\text{La}(\text{OH})_3$, and LaOOH in ref 25 are also shown in Figure 4. Obviously, the nanoscale samples have a lower ratio of signal-to-noise compared with bulk because of their tiny sizes and larger structural disorder, as well as the mixture of multiple

phase. But the EXAFS oscillations are still somewhat similar between sample (a), (b), and $\text{La}(\text{OH})_3/\text{LaOOH}$, or sample (b), (c), and Mn_2O_3 .

Figure 4c,d shows the Fourier transform spectra of k^3 -weighted EXAFS curve for La L_3 -edge and Mn K-edge. From Figure 4c, it can be seen that the FT spectra of sample (a) and (b) have obviously different characteristics with others and are very similar to that of $\text{LaOOH}/\text{La}(\text{OH})_3$.²⁵ This difference is consistent with XRD patterns and XANES spectra. The first coordination peak is from the La–O contribution, whereas the second coordination peak includes the La–O, La–Mn, and/or La–La contribution. In sample (a) and (b), the first peak is dominant, the second peaks have the maximum magnitude in sample (d) and (e), while sample (c) is in the intermediate states. It is identified that a structural change surrounding central La atoms occurs around the annealing temperature 600°C .

For the Mn K-edge as shown in Figure 4d, all the first peaks are similar to each other with almost no change in shape and position. However, an obvious change of the second coordination peaks illustrates that the higher coordination shells surrounding Mn are more affected by the annealing temperature. The structural transformation from Mn oxides to $\text{LaMnO}_{3+\delta}$ took place also around 600°C . Sample (c) has a different second coordination peak from samples (d) and (e) but similar to sample (b), which means that the local atomic structure around Mn centers in sample (c) is quite similar to sample (b). It corresponds to the unfinished phase change from the Mn oxides to $\text{LaMnO}_{3+\delta}$. The Mn K-edge FT spectrum of bulk Mn_2O_3 is also shown in Figure 4d. It can be found that the second-peak position of sample (c) is almost the same as that of Mn_2O_3 , which implies that sample (c) contains at least a Mn_2O_3 -like contribution. In other words, sample (c) is probably a mixture of Mn_2O_3 and $\text{LaMnO}_{3.12}$. In addition, we also note that the change direction of Mn K-edge is in good agreement with that of La L_3 -edge.

The EXAFS spectrum of La L_3 -edge was fitted by using a single-shell model for sample (a) due to the limitation of the free parameters. It was about 7 oxygen atoms surrounding La with an average La–O bond length of 2.48 \AA . This is very similar to the local atomic structures in crystalline LaOO ,²⁶ in which 7 oxygen atoms were slightly separated into 5 subshells with the average bond length of 2.484 \AA . Although the diffraction pattern of sample (b) is similar to bulk $\text{La}(\text{OH})_3$ with $P63/m$ space group with the exception of the broadening of the diffraction peaks, a single-shell fitting was tested and could not give reasonable structural parameters. Obviously, although sample (b) is not a pure $\text{La}(\text{OH})_3$, it still includes the contribution from the as-prepared sample (a). We considered that sample (b) consists of two parts; the crystalline part as shown by the XRD pattern and the amorphous one that is similar to the as-prepared sample (a). A double-phase model was applied to fit the EXAFS spectrum of sample (b) with one phase as the crystalline part fixed to be 2.57 \AA according to the $\text{La}(\text{OH})_3$ crystal structure¹⁴ and its Debye–Waller factor was also calculated and fixed according to the Einstein model. The content of the crystalline part can be estimated to be about 22% based on the nominal coordination number and the crystal structure. Therefore, there is still about 78% atoms in the amorphous part. The real coordination number around La in the amorphous part can be calculated to be about 7.0 according to the content of 78% and the nominal coordination number of 5.6. The 7 oxygen coordination atoms around La was found located at about 2.47 \AA in the amorphous part, which is almost the same with local atomic structures in the amorphous

TABLE 1: Local Structural Parameters around La and Mn Central Atoms in the Nanomaterials^a

sample	La L ₃ -edge				Mn K-edge				
	bonds	<i>N</i>	<i>R</i> (Å)	$\sigma^2(\times 10^{-3})$	bonds	<i>N</i>	<i>R</i> (Å)	$\sigma^2(\times 10^{-3})$	$\sigma^{(3)}(\times 10^{-4})$
(a)	La–O	7.1 ± 0.6	2.48 ± 0.02	8.4 ± 3.5 11.0 ± 3.1	Mn–O	2.3 ± 0.4	1.86 ± 0.02	0.9 ± 3.0	
(b)	La–O	5.6 ± 0.6	2.47 ± 0.02		Mn–O	3.7 ± 0.4	1.95 ± 0.02	1.1 ± 3.2	
	La–O	1.9 ± 0.4	2.57	4.1	Mn–O	2.4 ± 0.5	1.85 ± 0.02	2.1 ± 3.4	
(c)	La–O	4.5	2.57	4.6 ± 2.6	Mn–O	3.6 ± 0.5	1.95 ± 0.02	1.9 ± 2.2	
	La–O _I	1.5	2.34	3.6 ± 3.6					
	La–O _{II}	3.0	2.76	12.0 ± 4.6	Mn–O	2.8 ± 0.4	1.89 ± 0.02	3.9 ± 3.4	
	La–O _{III}	1.5	3.18	3.6 ± 3.6	Mn–O	2.9 ± 0.4	1.98	11.0 ± 3.7	
	La–Mn	3.0 ± 0.6	3.367	8.8 ± 3.6					
	La–La	3.0 ± 0.6	3.886	8.3 ± 3.4					
	La–O	1.8	2.57	3.1 ± 2.6					
(d)	La–O _I	2.4	2.34	2.2 ± 3.6					
	La–O _{II}	4.8	2.76	8.8 ± 4.2	Mn–O	1.3 ± 0.3	1.89 ± 0.02	2.2 ± 3.4	
	La–O _{III}	2.4	3.18	2.2 ± 3.6	Mn–O	4.7 ± 0.4	1.98	5.0 ± 3.2	
	La–Mn	6.1 ± 0.6	3.367	8.8 ± 3.2					
	La–La	5.2 ± 0.6	3.886	9.0 ± 3.6					
	La–O _I	3.0	2.34 ± 0.02	2.0 ± 3.6					
	La–O _{II}	6.0	2.76 ± 0.02	7.6 ± 4.3					
(e)	La–O _{III}	3.0	3.18 ± 0.02	2.0 ± 3.6					
	La–Mn	8.0	3.367	8.0 ± 2.6	Mn–O	6.1 ± 0.4	1.98 ± 0.02	5.8 ± 3.7	4.5 ± 2.7
	La–La	6.0	3.886	9.0 ± 3.4					

^a *N* is the coordination number, *R* is the interatomic distance, σ^2 is the relative Debye–Waller factor, and $\sigma^{(3)}$ is the third cumulant.

as-prepared sample (a). For Mn–K edge in samples (a) and (b), a single-shell model cannot also give reasonable structural parameters, which implies that the local structures around Mn diverge from the single-shell model. The fitting results demonstrated that there are about 6 oxygen atoms around Mn, and they are separated into two subshells in sample (a) and (b) as listed in Table 1.

On the basis of the XRD patterns, the main crystalline phases in sample (c), (d), and (e) have almost the same structure of LaMnO_{3+δ} with *R*-3*c* space group. In this case, the La–O and Mn–O bond lengths can be expressed as eq 1, which are only dependent on the lattice parameters *a* and *c* as well as the oxygen atomic coordinates *x*. They are only correlated with the lattice parameters *a* and *c*, particularly for La–Mn and La–La bond lengths. From the known lattice parameters *a* and *c*, we obtained that the La–Mn_I, La–Mn_{II} and La–La bond lengths are 3.332 Å, 3.377 Å, and 3.886 Å, respectively. While for the three La–O subshells, the sum of La–O_I and La–O_{III} bond lengths is equal to the lattice parameter *a*, the La–O_{II} bond length is correlated with *x*. In the reference,¹⁵ the *x* value is reported to be 0.551, and the La–O_{II} bond length changes in the range 2.74–2.77 Å if *x* is changed in the range 0.52–0.58.

$$\begin{cases} \text{La–O}_I = a(1 - x) \\ \text{La–O}_{II} = \sqrt{(x^2 - x + 1/3)a^2 + c^2/36} \\ \text{La–O}_{III} = ax \end{cases}$$

$$\begin{cases} \text{La–Mn}_I = c/4 \\ \text{La–Mn}_{II} = \sqrt{a^2/3 + c^2/144} \end{cases} \quad (1)$$

$$\text{La–La} = \sqrt{a^2/3 + c^2/36}$$

$$\text{Mn–O} = \sqrt{(x^2 - x + 1/3)a^2 + c^2/144}$$

In fact, samples (c), (d), and (e) are composed of the crystalline LaMnO_{3+δ}, the crystalline La(OH)₃, and the amorphous Mn oxides. But the contents of La(OH)₃ and Mn oxides in sample (e) are negligible as indicated by the XRD pattern. Therefore, an asymmetrical atom-pair model with the third cumulant $\delta^{(3)}$ was used to fit the Mn K-edge EXAFS spectrum

of sample (e). But there are a total of 6 bond lengths located in the range of 0.98–3.84 Å around central La atoms in sample (e), which cannot be well isolated in the La L₃-edge FT's. In our EXAFS data analysis, both La–Mn_I and La–Mn_{II} subshells were described as an averaged shell. On the other hand, due to the correlation of La–O_I and La–O_{III} the two subshells were set to have the same Debye–Waller factors and shifts of energy threshold. Thus, 5 shells (11 fitting parameters) were used. All the 5 bond lengths were correlative according to the crystalline structure as listed in eq 1, and the lattice parameters *a* and *c* were determined from the XRD pattern. Finally, only the *x* value or the La–O_{II} bond length, the Debye–Waller factors, and the shifts of energy threshold need to be fitted. The best fitting results are listed in Table 1. The *x* value was calculated to be 0.573 based on the fitting Mn–O bond length. This is consistent with that value calculated from the three La–O bond lengths.

For the Mn K-edge of samples (c) and (d), the single Mn–O shell cannot get reasonable fitting parameters. This implies that Mn atoms in sample (c) and (d) probably locate in two phases. Thus, a two-shell model was used to fit the Mn K-edge data of samples (c) and (d). One Mn–O bond length was fixed at the same value as in sample (e), which stands for the contribution from the crystalline LaMnO_{3+δ} phase. Another Mn–O shell represents the amorphous Mn oxides phase. The best fitting parameters are also shown in Table 1. According to the nominal coordination numbers, the content of the crystalline LaMnO_{3+δ} phase in sample (c) and (d) was calculated to be about 50 and 80%, respectively. The real coordination number of the amorphous Mn oxides is about 6. Our fitting results demonstrate that the amorphous Mn oxides have the similar local structures with crystalline Mn₂O₃.

For La L₃-edge, the spectra of samples (c) and (d) are the mixed contribution of the crystalline LaMnO_{3+δ} and La(OH)₃. According to the chemical components in sample preparation, the transformation ratio from La(OH)₃ to LaMnO_{3+δ} should be the same as that from Mn oxides to LaMnO_{3+δ}. The latter has been determined from the Mn K-edge analysis. An additional La–O shell was added to describe the contribution from La(OH)₃ phase in the La L₃-edge fitting of samples (c) and (d). Because of the limitation of the allowable fitting parameters, all the La–O coordination numbers were fixed at their respective

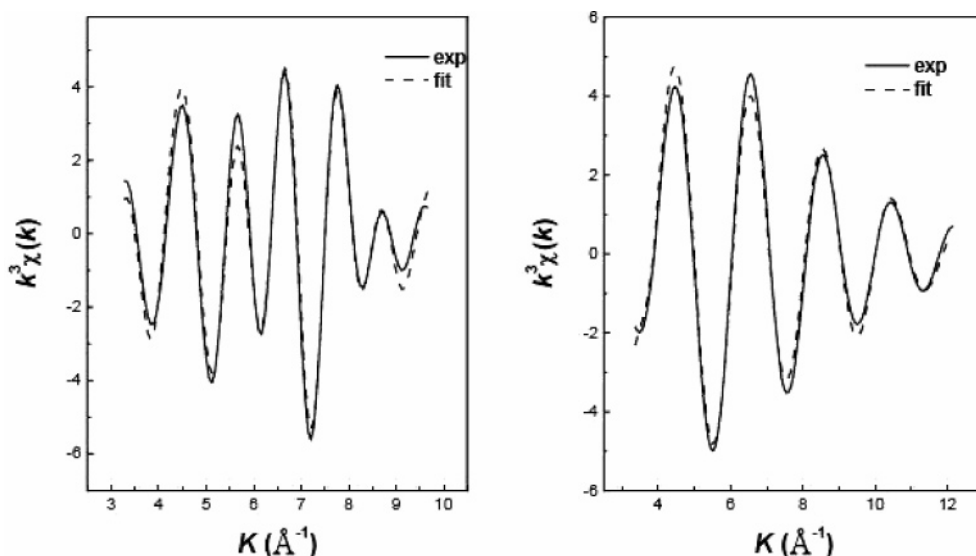


Figure 5. Experimental (solid line) and fitting EXAFS curve (dashed line) for La L_{3-} edge (left) and Mn K-edge (right) for sample (d).

coordination numbers in compounds $\text{La}(\text{OH})_3$ or $\text{LaMnO}_{3+\delta}$ and the phase contents were also fixed at the values obtained from Mn K-edge data analysis. It is well known that the average coordination number decreases with the nanoparticle size decreasing, but the oxygen coordination number around the metal center is always easy to keep the same value as in bulk. This is because the oxygen atoms are easily compensated from the air. That is why we can fix the oxygen coordination number as in bulk and only need to consider the phase contents for the La–O or Mn–O coordination in samples (c) and (d). However, the La–Mn and La–La coordination numbers will decrease with the nanoparticle size decreasing. In the fitting of samples (c) and (d), the La–Mn and La–La coordination numbers are allowed to be changeable. The final fitting results are also listed in Table 1. As examples, the fitting curves of La L_{3-} and Mn K-edge for sample (d) are shown in Figure 5.

For a nanoscale filament-like and sphere-like sample, if the radius of their nanoparticles is 5 times longer than the bond length, the coordination numbers can be expressed as²⁷ $N_{\text{nano}} = (1 - 3r/4R)N_{\text{bulk}}$. Here, r is the bond length and R is the radius of the nanofilaments or particles. According to this formula and the transformation ratio, the La–Mn and La–La coordination numbers were evaluated to be 3.6 and 3.5, respectively, for sample (c). However, as shown in Table 1, the La–Mn and La–La coordination numbers of sample (c) obtained from EXAFS measurements are less than the evaluated ones. Obviously, the existence of the nonstoichiometric oxygens induce the La and Mn vacancies, which results in the difference between the experimental results and the evaluated ones for the La–Mn and La–La coordination numbers. On the other hand, the existence of the impurity phase in the nanowires will also make us overestimate the radius of the pure $\text{LaMnO}_{3+\delta}$.

All the samples were heated at a different temperature but their XRD patterns and EXAFS spectra were collected at room temperature. Therefore, we think all samples have the same thermal disorders and the difference of Debye–Waller factors shown at the EXAFS data analysis are the only contribution from the structural disorder (or static disorder). As we expected, sample (c) has the biggest Debye–Waller factors. Obviously, this is corresponding to the phase transition from $\text{La}(\text{OH})_3/\text{Mn}$ oxides to $\text{LaMnO}_{3+\delta}$ around 600 °C. Although samples (c), (d), and (e) are all the mixtures of $\text{La}(\text{OH})_3$, Mn oxides, and $\text{LaMnO}_{3+\delta}$, the contents of sample (c) are the nearest to 50:50. The coexistence of several components will cause the lattice

mismatch, distortions, and defects between the phase interfaces, which results in larger structural disorders or the increase of the Debye–Waller factor. With the annealing temperature increasing, more and more parent phases $\text{La}(\text{OH})_3$ and Mn-compounds were transformed to the final compound $\text{LaMnO}_{3+\delta}$. Because the annealing temperature is not high enough and the heating time is not long enough, finally there are slight reminders of $\text{La}(\text{OH})_3$ and Mn oxides that survived in the $\text{LaMnO}_{3+\delta}$ for samples (c), (d), and (e). With the reminder decreasing and the interface between $\text{LaMnO}_{3+\delta}$ and $\text{La}(\text{OH})_3$ or Mn-oxides decreasing, the distortion and defects are partly removed. Therefore, the static disorder or structural disorder decreases with increasing annealing temperature.

Conclusion

In this paper, the $\text{LaMnO}_{3+\delta}$ nanomaterials were prepared by using a chemical method. The as-prepared sample was, respectively, heat-treated at 180, 600, 800, and 900 °C, which accompanies a change of particle shape from nanofilament to sphere as shown in the TEM photograph, as well as the phase transformation from amorphous LaOOH and MnOOH to crystalline $\text{La}(\text{OH})_3$ and some amorphous Mn_2O_3 -like compounds, then to crystalline $\text{LaMnO}_{3+\delta}$. Atomic structures in these samples were studied by using EXAFS and XRD techniques. Our experimental results demonstrate that the crystalline $\text{La}(\text{OH})_3$ is first formed in the as-prepared amorphous nanowires and were embedded in amorphous Mn_2O_3 -like compounds. With the annealing temperature increasing, the crystalline structure of $\text{La}(\text{OH})_3$ collapses by losing the water and reacts with the surrounding Mn_2O_3 -like compounds to form $\text{LaMnO}_{3+\delta}$. It was the structural collapse that resulted in a radial growing-up, as well as the shape change from nanowire to nanorod, then to nanosphere. The atomic structures in the annealing process are barely changed, but the phase contents are changeable with annealing temperature. All these results are useful to understand the mechanism of nanomaterial formation and to control the nanomaterials shape.

Acknowledgment. This work is supported by the National Natural Science Foundation of China with No. 10374087. This work is also partly supported by the States Key Project for Fundamental Research (2003CB716900) and National Center for Nanoscience and Technology, China, the National Outstand-

ing Youth Fund (10125523), the Key Important NanoResearch Project of the National Natural Science Foundation of China (90206032), and the Knowledge Innovation Program of the Chinese Academy of Sciences (KJCX2-SW-N11, KJCX2-SW-H12-02).

References and Notes

- (1) *Properties and Applications of Perovskite-Type Oxides*; Tejuca L. G., Fierro J. L. G., Eds.; Dekker: New York, 1993.
- (2) *Structure-Property Relationship in Perovskite Electroceramics. Perovskite: A structure of Great Interest to Geophysics and Material Science*; Newman R. E., Navrotsky A., Weidner D. J., Eds.; American Geophysical Union: Washington, D.C, 1989; p 66.
- (3) Voorhoeve R. J. H. In *Advanced Materials in Catalysis*; Academic Press: New York, 1977; p 129.
- (4) Voorhoeve R. J. H. In *Advanced Materials in Catalysis*; Burton, J. J., Garten, R. L., Eds.; Academic Press: New York, 1977; p 129.
- (5) Seiyama T. *Catal. Rev.—Sci. Eng.* **1992**, *34*, 281.
- (6) Tejuca, L. G.; Fierro, J. L. G.; Tascon, J. M. D. *Adv. Catal.* **1989**, *36*, 237.
- (7) Saracco, G.; Scibilia, G.; Iannibello, A.; Baldi, G. *Appl. Catal. B* **1996**, *8*, 229.
- (8) Toeld, B. C.; Scott W. R. *J. Solid State Chem.* **1974**, *10*, 183–194.
- (9) Subias, G.; Garcia, J.; Blasco J.; Proietti M. G. *Phys. Rev. B* **1998**, *58*, 2987–2993.
- (10) Van Roosmalen, J. A. M.; Cordfunke, E. H. P.; Helmholdt, R. B.; Zandbergen, H. W. *J. Solid State Chem.* **1994**, *110*, 100–105.
- (11) Van Roosmalen, A. M.; Cordfunke E. H. P. *J. Solid State Chem.* **1994**, *110*, 106–108.
- (12) Ritter, C.; Ibarra, M. R.; De Teresa, J. M.; Algarabel, P. A.; Marquina, C.; Blasco, J.; Garcia, J.; Oseroff, S.; Cheong, S.-W. *Phys. Rev. B* **1997**, *56*, 8902–8911.
- (13) Ressler, T. WinXAS: A XAS Data Analysis Program under MS Windows. *J. Synchrotron Radiat.* **1998**, *5*, 118–122.
- (14) Beall, G. W.; Milligan, W. O.; Wolcott, H. A. *J. Inorg. Nuclear Chem.* **1977**, *39*, 65–70.
- (15) Cheetham, A. K.; Rao, C. N. R.; Vogt, T. *J. Solid State Chem.* **1996**, *126*, 337–341.
- (16) Rehr, J. J.; Albers, R. C.; Zabinsky, S. I. *Phys. Rev. Lett.* **1992**, *69*, 3397–3400.
- (17) Zabinsky, S. I.; Rehr, J. J.; Ankudinov, A.; Albers, R. C.; Eller, M. J. *Phys. Rev. B* **1995**, *52*, 2995.
- (18) Tang, B.; Ge, J. H.; Wu, C. J.; Zhuo, L. H.; Niu, J. Y.; Chen, Z. Z.; Shi, Z. Q.; Dong, Y. B. *Nanotechnology* **2004**, *15*, 1273–1276.
- (19) Adachi, T.; Noji, T.; Koike, Y. *Phys. Rev. B* **2001**, *64*, 144524.
- (20) Chen, C. T.; Lin, B. N.; Hsu, Y. Y.; Liao, J. D.; Cheng, W. H.; Lin, C. Y.; Ku, H. C.; Lee, J. F.; Jang, L. Y.; Liu, D. G. *Phys. Rev. B* **2003**, *67*, 214424.
- (21) Hirofumi, A.; Hiroyuki, Y.; Takashi, Y.; Tsunehiro, T.; Seiichiro, I. *J. Synchrotron Radiat.* **2001**, *8*, 593–595.
- (22) Natoli, C. R. In *EXAFS and Near Edge Structure*; Springer Series in Chemistry and Physics; Bianconi, A., Incoccia, L., Stipcich, S., Eds.; Springer: Berlin, 1983; Vol. 27, p 43.
- (23) Francois, F. *Phys. Rev. B* **2005**, *71*, 155109.
- (24) Dish, D. L.; Post, J. E. *Am. Mineral.* **1989**, *74*, 177–186.
- (25) Ali, F.; Chadwick, A. V.; Smith, M. E. *J. Mater. Chem.* **1997**, *7*, 285–291.
- (26) Klevtsov, P. V.; Sheina, L. P. *Neorg. Mater.* **1965**, *1*, 2219–2226.
- (27) Calvin, S.; Miller, M. M.; Goswami, R.; Cheng, S.-F.; Mulvaney, S. P.; Whitman, L. J.; Harris, V. G. *J. Appl. Phys.* **2003**, *94*, 778.